

**Assessment of hemodynamic conditions in the aorta following root
replacement with composite valve-conduit graft**

Zhuo Cheng¹, Emaddin Kidher², Omar A. Jarra², Declan P O'Regan³, Nigel B.
Wood¹, Thanos Athanasiou², Xiao Y. Xu¹

¹Department of Chemical Engineering, Imperial College London, South Kensington
Campus, London SW7 2AZ, UK

²Department of Surgery and Cancer, Imperial College London, St. Mary's Hospital,
London W2 1NY, UK

³Institute of Clinical Science, Imperial College London, Hammersmith Hospital,
London W12 0HS, UK

Correspondence:

Xiao Yun Xu

Department of Chemical Engineering

Imperial College London

South Kensington Campus

London SW7 2AZ

Tel: +44 207 594 5588

E-mail: yun.xu@imperial.ac.uk

Abstract

This paper presents the analysis of detailed hemodynamics in the aortas of four patients following replacement with a composite bio-prosthetic valve-conduit. Magnetic resonance (MR) image-based computational models were set up for each patient with boundary conditions comprising subject-specific three-dimensional inflow velocity profiles at the aortic root and central pressure waveform at the model outlet. Two normal subjects were also included for comparison. The purpose of the study was to investigate the effects of the valve-conduit on flow in the proximal and distal aorta. The results suggested that following the composite valve-conduit implantation, the vortical flow structure and hemodynamic parameters in the aorta were altered, with slightly reduced helical flow index, elevated wall shear stress and higher non-uniformity in wall shear compared to normal aortas. Inter-individual analysis revealed different hemodynamic conditions among the patients depending on the conduit configuration in the ascending aorta, which is a key factor in determining post-operative aortic flow. Introducing a natural curvature in the conduit to create a smooth transition between the conduit and native aorta may help prevent the occurrence of retrograde and recirculating flow in the aortic arch, which is particularly important when a large portion or the entire ascending aorta needs to be replaced.

Key Terms: Aortic root replacement, patient-specific modelling, phase-contrast MRI, helical flow, wall shear stress, computational fluid dynamics

Introduction

Aortic valve disease (AVD) is a common and highly prevalent disease process affecting millions of people worldwide.³⁴ It is associated with elevated mortality and morbidity and represents an increasing public-health problem due to its association with ageing populations.²⁷ AVD is most commonly caused by age-related progressive calcification, congenital abnormalities (such as bicuspid aortic valve) and rheumatic fever. This may lead to the development of functional aortic stenosis and/or regurgitation³³ and can be associated with progressive aortic dilatation, aneurysm formation, dissection and other vascular related end-organ effects.¹¹

The gold-standard surgical procedure for replacement of the aortic root and ascending aorta is the modified Bentall procedure, which involves replacement of native tissue with a pre-fabricated composite valve-conduit. Since the first root replacement with a valve-conduit in 1968,² prosthesis design has improved considerably. Despite these improvements, no current conduit is comparable to native healthy tissue and limitations include impaired long-term durability, reduced hemodynamic performance, thrombogenicity and a risk of bleeding (especially with mechanical prostheses).^{4,14,29} These issues have led to demand from patients and clinicians for better clinical outcomes and have motivated manufacturers to produce more advanced designs.

In 2006, a new prefabricated composite bio-prosthetic valved conduit graft was introduced to the market. The BioValsalvaTM (Vascutek Terumo, Renfrewshire, Scotland) comprises a stentless porcine aortic valve, the Elan valve (VascutekelanTM) which is pre-sewn to a self-sealing triple-layered hemostatic vascular graft (Vascutek TriplexTM). The graft incorporates sinuses of Valsalva (mimicking the anatomy of the

aortic root), which theoretically leads to better coronary artery flow.¹⁹ Preliminary clinical experience has shown promising short-term results in terms of mortality, morbidity, cross-clamp times, haemostasis and ease of use.^{3,10,15,19} However, no detailed study of the hemodynamic performance of BioValsalvaTM has been made previously.

Cardiovascular magnetic resonance (CMR) imaging with phase-contrast velocity mapping allows for noninvasive evaluation of flow patterns in the aortic root and aorta.^{1,17,23,26,36} Previous studies have used CMR to quantify hemodynamic performance of normal and diseased native valves, as well as different bioprosthetic valves.^{1,23,36} These have mainly focused on spatiotemporal patterns of axial flow components in the proximity of the valves.^{1,36} Time-resolved three-directional MR velocity mapping can be used to obtain flow patterns in the aorta. Combined with flow visualization methods, 3D flow streamlines, pathlines and wall shear stress can also be derived.^{8,17,23,26,} However, the spatial and temporal resolution of MR imaging is a limiting factor in providing accurate evaluation of hemodynamic parameters such as wall shear stress and particle residence time. Computational fluid dynamics (CFD) is a powerful noninvasive analysis tool, giving comprehensive insight into complex flow phenomena. Based on patient-specific geometry and functional boundary conditions acquired from medical images, CFD modelling allows quantitative assessment of the hemodynamic environment in different clinical conditions with good accuracy.³⁵

The BioValsalvaTM conduit replaces the aortic valve, root and part of the ascending aorta.^{3,10,15,19} After the procedure, the flow distal to the valve as well as the morphology of the aortic root and ascending aorta can be altered, which may influence flow in the coronary arteries and the remaining aorta.⁹ This is of high

clinical relevance as these changes could have an impact on overall organ perfusion and may affect other processes such as the endothelial function of the aorta. The current study represents a first detailed investigation of aorta hemodynamics following root replacement with the BioValsalvaTM valve-conduit, together with a comparative analysis of normal aortas.

Materials and Methods

Subjects

Four patients and two volunteers were included. Patients were between 60-65 in age and were all male, white Caucasians who underwent implantation of a BioValsalvaTM graft (Fig. 1a). For comparison, two healthy volunteers (with no medical history, including that of coronary/valvular disease) were recruited as a control group with race, gender and age matching. Ethical approval (10/H0717/45) was granted and informed consent was obtained from all participants prior to inclusion. The study complied with the Declaration of Helsinki. The two normal subjects were referred to N1 and N2, and the four patients were indicated as P1 to P4 in sequence.

Cardiovascular Magnetic Resonance Imaging

Cardiac MR was performed on a 1.5T Philips Achieva system (Best, Netherlands) at the Robert Steiner MRI Unit at Hammersmith Hospital (London, UK). Patients were imaged at four weeks after the surgery. The MR image acquisition included anatomic and phase contrast images. Multislice sagittal anatomic images were obtained using a navigator-gated balanced steady state free precession angiogram covering the whole thoracic aorta including the proximal great vessels (voxel size $0.5 \times 0.5 \times 2$ mm). 2D phase contrast (PC) images were acquired orthogonal to the aortic axis

with velocity encoding gradients in the foot-head (FH), anterior-posterior (AP) and right-left (RL) directions at the level of the annulus, and in the descending thoracic aorta, at the level of pulmonary bifurcation. The velocity encoding parameter (V_{enc}) was adjusted to be 10% above the peak velocity for each component of flow (in-plane pixel resolution 1.4 mm, slice thickness 10 mm). Images were obtained using retrospective cardiac gating with reconstructions of 100 time points in an average cardiac cycle (temporal resolution 33 ms).

Anatomic Image Processing and Geometry Reconstruction

The aorta was reconstructed from the MR images via Mimics 16 (Materialise HQ, Louvain, Belgium), from the sinus to the mid-descending aorta, including the arch branches; other small branches on the descending aorta were excluded. The geometry reconstruction procedure included steps of segmentation and 3D reconstruction, followed by an iterative surface smoothing algorithm. To check the accuracy of reconstruction, the final geometry of each subject was projected to the original anatomic MR images and the geometry boundaries were examined on each of the serial images. The reconstructed aortas for the normal subjects and patients are presented in Fig.1b and 1c respectively.

Flow Image Analysis

An in-house MATLAB programme was used to obtain time-varying velocity maps from the PC-MR images.⁷ The magnitude image was segmented first to obtain the lumen contour, which was then mapped on to the corresponding phase image to locate the target flow field. The velocity map within the area was calculated based on the velocity encoding algorithm of the PC sequence for each of the three velocity components. The velocity profiles, in FH, AP and RL, provided a complete

description of the 3D flow pattern at the imaging plane with both through-plane and in-plane velocity components. Volumetric flow was calculated by integrating velocity map over the corresponding cross-section of the aorta at each of the 100 available time points during a cardiac cycle, yielding volumetric flow waveforms at the aortic root and descending thoracic aorta. The spatiotemporal velocity profiles in three orthogonal components at the aortic root are presented in Fig. 2 for each subject.

Aortic Pressure Waveform Acquisition

Pressure measurements were made on all the subjects within 30 minutes prior to the MR scans by using a BP Plus device (BP Plus, Uscom, Australia). Systolic and diastolic brachial blood pressures from the pressure cuff on the left upper arm were acquired, followed by a suprasystolic measurement recording intra-arterial pressure oscillations in the brachial artery.²² Using a physics-based model of the left subclavian-to-brachial branch, the total pressure waveform at the aorta was obtained.²² The measurement was repeated twice for each subject, and the average values were employed in the computational model. All the subjects were required to remain still and quiet (under resting conditions) during the measurement. The obtained aortic pressure waveforms for all the subjects examined are also included in Fig. 2.

Computational Model and Flow Simulation

The computational model was based on the reconstructed aorta geometry and boundary conditions derived from MR images and pressure measurement. The inlet was located at the PC-MR imaging plane at the aortic root, where the spatial velocity profile was mapped by coordinate transformation from the 2D image plane to 3D global coordinates. A coordinates-transfer matrix was set up between the MR

velocity image and the inlet of the 3D computational model. Each pixel in the velocity map corresponded to a point at the inlet based on a transformation matrix calculated from four pairs of corresponding reference points between the segmented velocity map and the inlet plane. Linear interpolation was performed in space (between pixels) and in time (between the 100 available time points). Velocity maps in RL, AP and FH directions were projected to the inlet in x, y and z Cartesian coordinates respectively.

The outlet boundary was located at the level of diaphragm, defined as an 'opening boundary' with the measured pressure waveform. The exits of the three branches on the aortic arch, perpendicular to the respective vessel centreline, were specified as 'outlet boundaries', located approximately 50 mm from the branch origins on the arch. Mass flow rate was applied at the branch outlets, based on distribution according to their relative cross-sectional areas³⁷ and the total flow rate of the three branches; the latter was calculated as the difference in systolic-average flow rate between the aortic root and thoracic descending aorta. Walls were assumed rigid with no-slip.

The geometry constrained by the specified boundaries was then imported into a mesh generation package, ANSYS ICEM CFD 15 (ANSYS Inc, Canonsburg, PA), with which structured mesh was generated. Very fine resolution of hexahedral elements was ensured in the near wall region with the dimensionless height of wall cells (y^+) being less than 1 for compliance with the low-Reynolds number transitional flow model adopted.¹⁸ Mesh independence tests were carried out for each subject by comparing results obtained with different mesh densities. The final adopted mesh varied between 1.5-2.0 million elements depending on the size of the model. All simulations reported in this study were implemented in ANSYS CFX 15 (ANSYS Inc, Canonsburg, PA), within which a high order advection scheme was chosen for spatial discretisation of the Navier-Stokes equations and a second-order implicit

backward Euler scheme for temporal discretisation. The blood was treated as a Newtonian with a dynamic viscosity of 0.004 Pa·s and density of 1060 kg/m³. A fixed time-step of 0.001s was adopted and the maximum RMS residual of 10⁻⁶ was set as the convergence criterion. The simulation results were analysed using ANSYS CFX-Post 15 and CEI Enight 10 (CEI Inc., Apex, NC, USA).

Quantities of Interest

A number of wall shear stress (WSS) related parameters were analysed; these included time-averaged wall shear stress (TAWSS), oscillatory shear index (OSI) and shear range index (SRI). Definitions of TAWSS and OSI are standard and have been adopted widely, hence are not repeated here. SRI is a parameter which measures WSS asymmetry along the circumference of the lumen, reflecting flow inhomogeneity at the vessel wall.¹ SRI was calculated for a series of planes along the vessel, based on the following definition:¹

$$SRI = \frac{\max[\tau_{\max}(\theta, t) - \tau_{\min}(\theta, t)]}{\tau_{t-avg}} \quad (1)$$

where $\tau_{\max}(\theta, t)$ and $\tau_{\min}(\theta, t)$ are the maximum and minimum instantaneous WSS around the selected circumference in one cardiac cycle, and τ_{t-avg} is the temporal and circumferentially averaged WSS at the same location. SRI represents the maximum range of the local WSS normalized by the averaged WSS.

To further understand the complex flow patterns in the aorta, several indices for helical flow quantification were adopted in this study. Helical flow index (HFI)^{12, 31}, a descriptor of helical structure, can be obtained by calculating local normalized helicity (LNH) from a particle trace analysis of the flow.

$$LNH(s; t) = \frac{V(s; t) \cdot \omega(s; t)}{|V(s; t)| \cdot |\omega(s; t)|} \quad -1 \leq LNH \leq 1, \quad (2)$$

where s is the location and t is the time. The sign of LNH indicates the direction of rotation of flow, which is positive for clockwise (CW) rotation, and negative for counter-clockwise (CCW) rotation.

Based on the recorded LNH on the trajectory of each particle, the time-averaged value of LNH experienced by the k th particle moving along its trajectory during a specified time interval can be evaluated as:³¹

$$hfi_k = \frac{1}{(T_k^{end} - T_k^{start})} \int_{T_k^{start}}^{T_k^{end}} |LNH_k(\zeta)| d\zeta \quad 0 \leq hfi_k \leq 1, \quad (3)$$

For a total of N_p particles moving in the flow domain, the HFI can be calculated as:

$$HFI = \frac{1}{N_p} \sum_{k=1}^{N_p} hfi_k \quad 0 \leq HFI \leq 1, \quad (4)$$

In addition, the mean value of HFI can be calculated over the particle sets obtained from a number of injection time points N_T for each subject:

$$\overline{HFI} = \frac{1}{N_T} \sum_{j=1}^{N_T} HFI_j \quad 0 \leq \overline{HFI} \leq 1, \quad (5)$$

Results

Morphologic parameters

As shown in Fig.1, the aortic root replacement with a valve-conduit altered the geometry of the root and ascending aorta. Basic geometric parameters, including

cross-sectional area and aortic diameter, have been analysed and reported previously.¹⁶ Two additional parameters, tortuosity and aortic angle, which relate to the 3D configuration of the aorta were examined and the results are summarised in Table 1. Values of tortuosity were calculated for the ascending aorta (conduit included for patients). It is defined as the actual length of the ascending aorta (measured along the centreline) divided by the straight line distance between the aortic root and left subclavian artery. The patient group showed lower tortuosity (except for P4 due to the sharp bend of the native ascending aorta) than the normal subjects. The angle between the conduit and the native ascending aorta/aortic arch was calculated for the patients by measuring the most acute angle between the centreline of the conduit and the aorta. P4 had the sharpest angle while P1 had the widest angle with a difference of 24 degrees. The angle between the aortic arch and the descending aorta was also measured and compared between normals and patients, with the patients displaying a sharper angle compared to the normals.

Flow Patterns

Instantaneous streamlines and velocity vector fields at predefined planes were displayed for qualitative examination of flow patterns. The representative streamlines were produced at peak systole and colour coded based on velocity magnitude, as shown in Fig. 3 for a normal subject. The vortical flow structure was interrogated with velocity vectors projected on selected planes perpendicular to the centreline of the aorta at six locations: 1) just distal from the aortic valve; 2) mid-way along the ascending aorta (normals) or at the distal anastomosis site where the conduit was joined with the native aorta (patients); 3) just proximal to the origin of the brachiocephalic artery; 4) on the arch between the left common carotid artery and the left subclavian artery; 5) distal arch; and 6) at the level of pulmonary bifurcation

in the descending aorta. The planes were visualized from the proximal side (viewed in the direction of forward flow) and were oriented so that the bottom side of the image corresponds to the inner curvature of the aorta. Flow patterns in N1 are shown in Fig. 3 where CW rotating vectors correspond to right-handed helicity and CCW vectors represent left-handed helicity (see later). Centres of vortices are marked by stars (*) on each plane. Fig. 4 shows peak systolic flow patterns for the four patients.

Flow patterns in N1 (Fig. 3) and N2 (not shown here) were similar to a typical pattern found in a normal aorta, with an initial jet of blood coming out of the valve being skewed toward the anterior right wall of the ascending aorta.¹³ About 1/3 of the aortic flow exited through the arch vessels, leaving a slower moving region taking up the space in the outer arch, before the flow was redistributed under the action of curvature-induced centrifugal pressure gradients as it entered the descending aorta. There was a small separated region on the inner surface of the distal arch, which is not uncommon. Two opposing vortices can be seen in the ascending aorta initially located near the left and anterior wall, with the vortex centres moving along the inner curvature, until the vortices separated as they entered the descending aorta.

In patients' aortas, the jet flow from the aortic valve in P1, P2 and P3 was skewed toward the inner curvature of the ascending aorta, while in P4 the flow impinged on the anterior right wall, depending on the shape and orientation of the conduit. Bi-helical flow structures, comprising one CW and one CCW vertex, could be found in the proximal ascending aorta in all four patients, but because of the varying shape, length and orientation of the conduit, the locations of the two vortices were near the anterior right wall in the first three patients and in the opposite area in P4. However, in P1 and P3 a third vortex centre was also present. At the anastomosis site (Plane

2), both vortices moved to the centre of aorta except in P2, where the conduit was connected to the native aorta just before the branching point of the brachiocephalic artery. The relatively straight geometry of the conduit caused the vortices to remain near the anterior right region in P2. Although the other three patients, P1, P3 and P4, had helical flow dominating the central aorta at the anastomosis region, the vortices moved toward the inner curvature, like the normals at Plane 3, before reaching the arch. Hence in the aortic arch, these three patients also presented right-handed helical flow inferiorly. Conversely, in P2, the anatomical feature of the conduit replacing the 'ascending aorta' caused the flow to skew toward the superior wall of the arch, and induced recirculating flow in the inferior region. In the descending aorta, helical flow was found mostly near the inner curvature of the aorta.

Helical Flow Index

A cluster of evenly distributed particles was released from the inlet at five chosen time points, of which T'1 is the starting time of systole and T'3 is peak systole; the intervals between each time point were the same. Fig. 5a presents the particle trace patterns for P1 from the five injection time points as indicated. The trajectories of the particle sets were colour coded to display the instantaneous value of LNH along the movement of particles in the aorta. The total traveling time of each particle in the fluid domain was between the injection time and the end of systole.

Fig. 5b shows the average values of HFI for the normal and patient groups at five particle injection times. The normal subjects had higher HFI values than the patients during systole. The maximum difference (28%) occurred at peak systole when the normal subjects had the largest value of HFI. Their lowest HFI was at the start of systole (T'1), with comparable values at systolic deceleration (T'4 and T'5), which

were slightly lower than at the mid-acceleration phase (T'2). In contrast with the normal subjects, the patient group presented the highest HFI at the mid-acceleration phase (T'2) and comparable values for peak and systolic deceleration phase (T'3, T'4 and T'5).

The mean value of HFI was calculated over the five particle sets, which represents for each subject the helical content within a streaming flow during the systolic phase (Fig. 5c). As can be seen, N1 had the highest value of $\overline{\text{HFI}}$ (0.42) among all the subjects, while N2 and the patient subjects P1 and P3 had a comparable value at 0.36. The other two patient subjects presented much lower values with P2 having the lowest at 0.27 and P4 at 0.32.

Wall Shear Stress

The TAWSS contours are shown in Fig. 6 where the same scale (between 0 and 7 Pa) was used for easy comparison, but the maximum TAWSS value varied among the subjects (see Table 1). For all the subjects, the three arch branches and junctions of the branches showed elevated TAWSS due to reduced arterial diameter and flow impingements. On the inner curvature of the aorta, normal subjects experienced high TAWSS in the aortic root where the aorta diameter decreased from the sinus to the ascending aorta. The highest value of TAWSS occurred at the branch junctions for normal subjects, while for patients it was mostly located in the conduit especially on the inner curvature approaching the distal anastomosis site. Among the four patients, P2 had an exceptionally large area of high TAWSS on the posterior wall of the conduit and aortic arch, and also experienced the highest value of TAWSS among all the subjects.

For quantitative comparisons of WSS-related parameters, TAWSS, OSI and SRI were calculated at 22 cross-sectional planes along the aorta for each subject. TAWSS and OSI were circumferentially averaged over each of the planes, referred as $TAWSS_{mean}$ and OSI_{mean} . Fig. 7 shows variations of the three parameters along the length of the aorta, which was segmented into ascending aorta (AAo), aortic arch (AA), descending aorta (DAo) for normals, with an additional BioValsalvaTM conduit (BV) section for patients. The averaged values for each section are summarised in Table 1. Corresponding to the spatial distribution of TAWSS in Fig. 6, the $TAWSS_{mean}$ curves for the patients demonstrated again high levels of TAWSS near the distal anastomosis site (BV–AAo/AA boundary). The normal subjects had the highest value of $TAWSS_{mean}$ around 4 Pa near the aortic root and also in the arch for N1. The patients had a similar range of $TAWSS_{mean}$ values in the descending aorta, among which P2 had a comparable value to N1, and the other patients had slightly lower value as N2. Based on the data analysed in Table 1, compared to normal subjects, the patients presented generally higher TAWSS on the conduit, ascending aorta and aortic arch while lower values in the descending aorta. On the other hand, the OSI_{mean} curves revealed that the highest value occurred in the thoracic descending aorta of all subjects.

Finally, values of SRI were compared. As shown in Table 1, normals had the highest SRI in the arch while patients had comparable SRI in the same arch section but much higher values in the conduit and ascending aorta sections. The descending aorta of patients also had slightly higher SRI compared to normals. Combining with the SRI curves in Fig. 7, it can be observed that P1 showed a similar variation range to N1 and N2, with an overall average value of around 10. However, P2 and P3 had high SRI above 20 (up to 60 in the arch of P3) in the conduit and ascending aorta.

Also, P3 and P4 showed much higher values of SRI (between 20 and 30) in the descending aorta than other subjects.

Discussion

This study has provided detailed information on peak systolic flow patterns and hemodynamic environment in post-operative aortas after BioValsalvaTM valve-conduit implantations, by using image-based CFD with subject-specific boundary conditions. Flow patterns through the valve and aortic root have been assessed and reported elsewhere.¹⁶ It was found that the conduits showed overall comparable functions of the aortic root and valve to their normal counterparts but had smaller orifice area, higher maximum velocity, and relatively large retrograde and secondary flow in the sinus. To examine further the influence of the valve-conduit on flow in the entire aorta, here we extended our analysis of detailed flow features and WSS indices to cover the range between the aortic root and the proximal descending aorta. Based on results for the normal and patient groups, this study has provided qualitative and quantitative comparisons in terms of flow pattern, helical flow structure and WSS related parameters. As the hemodynamic environment in the aorta has great clinical importance, these findings have potential implications for the design and implantation strategy of aortic valve-conduits.

The complexity of flow in the human aorta has long been acknowledged. PC-MRI technique enables non-invasive measurements of 3D flow velocities in the aorta.^{13, 30} Image-based CFD, on the other hand, has additional advantages in both spatial and temporal resolutions with highly resolved flow patterns, making it relatively easy to determine flow and other hemodynamic parameters.³⁵ However, a number of assumptions are usually made when combining in vivo imaging and CFD, of which,

the choice of inlet boundary conditions is crucial.^{32,35} Morbiducci et al.³² tested a number of commonly used inlet boundaries, and found that applying 3D MR flow profiles at the inlet led to more accurate description of the vortical flow structure in the aorta. In order to reproduce the aortic flow patterns as faithfully as possible, the computational models employed in this study were built from a comprehensive set of in vivo data, including patient-specific aortic anatomy, 3D flow velocity profiles at the inlet, and patient-specific aortic pressure waveform at the outlet. The latter is not expected to influence the flow pattern because of the rigid wall assumption, but will allow a more realistic estimation of the aortic pressure distribution.

Flow Structure and Helicity Content

Using MR velocity mapping, it has been found that paired or more vortices are a common flow feature in the ascending aorta of normals while a single vortex is more frequent in the arch.^{13, 17} Particle traces from PC-MRI of the human aorta³⁰ further revealed the presence of two opposing vortices in the ascending aorta and the disappearance of left-handed helical flow and persistence of right-handed helical flow in the arch. As in previous studies, the results presented here also showed two opposing vortices in the ascending aorta of normals and right-handed helical flow in the arch. However, there were more variations in patients. Flow patterns in three of the four patients showed some similarities to those of normals, including the onset of bi-helical flow in the proximal ascending aorta, but multiple cores of helical flow were present in the anastomosis region, owing to the abrupt angle between the conduit and distal aorta. Nevertheless, the bi-helical pattern was restored along the inner curvature of the arch, which was also observed in the normals.

Regarding the helical flow structure in terms of HFI, comparison of our results shown in Fig. 5a with the corresponding data in the literature³¹ suggested that the average value of HFI was in the normal range for two patients (P1 and P3) but lower in the other two patients (P2 and P4). The low HFI in P2 was likely attributed to the relatively straight conduit replacing the diseased ascending aorta, while the flat arch in P4 might have contributed to the low HFI in this case. As discussed earlier, helical flow is a common feature in normal aorta, which can influence the flow distribution to arch branches and help prevent flow recirculation. Helical flow plays a positive role in the vascular system, including reducing flow stagnation, improving oxygen transport between blood and arterial wall, as well as preventing the accumulation of atherogenic lipids on the inner wall of arteries.²⁵ Hence the clinical performance of vascular interventions including the aortic root replacement procedure examined in this study is expected to benefit from helical flow. Regarding the distribution of HFI at different time points, the highest value was found at peak systole for normals and in the mid-acceleration phase for patients. This differs from the PC-MRI derived results of Morbiducci et al.³¹ who found higher HFI in the deceleration phase of systole. Apart from geometry-related variations, this difference could also be caused by the rigid wall assumption in the CFD model and the different resolution of CFD results and PC-MRI data. Differences observed between normals and patients were most likely due to the lack of ascending aorta curvature and pointed velocity profiles with larger area of retrograde flow at the aortic root in patients.

WSS Related Parameters

Hemodynamic shear stress is known to affect endothelial cell functions,^{20, 21} and physiologically normal time-averaged WSS has been reported at approximately 1.5 to 2.0 Pa in human arteries.²⁸ However, little is known about the influence of WSS on

the synthetic surface of vascular prostheses. The BioValsalva™ vascular prosthetic conduit consists of three layers, with the inner layer being polyester. It has been reported that anastomotic intimal hyperplasia and surface thrombogenicity are responsible for the poor outcome of small to medium sized grafts, while large prostheses in the aorta have much better outcomes.³⁸ In view of this, the high TAWSS and moderate OSI values on the conduit in post-operative patients (Table 1), especially at the distal anastomosis, might help reduce the risk of thrombus formation on the surface. As a measure of circumferential asymmetry in wall shear, the value of SRI can be influenced by local geometric variations as well as flow profile from the valve, with jet impingement or skewed flow giving rise to high SRI.¹ As summarised in Table 1, the patient group had high average SRI in the conduit and the ascending aorta, while SRI values for the normal aortas were consistent with those reported by Barker et al.¹

Geometric Influence

Comparisons of flow patterns and hemodynamic parameters between the normal subjects and patients showed that P1 had the most similarity to normals, whereas the other post-operative modes showed obvious departure from the normal aorta. The pointed and skewed flow jet from the valve certainly contributed to the complexity and variety of the hemodynamic environment in the aorta; however this result also drew attention to the geometric features in the ascending aorta, particularly with regard to how the conduit is connected to the host aorta. The reconstructed post-operative aortas (Fig. 1) showed clearly that sharp angles were created between the relatively straight conduit and the distal ascending aorta, which had a strong influence on post-operative flow patterns in the ascending aorta and aortic arch. P2 differed from the other patients in that almost the entire ascending

aorta was replaced by the conduit, which was connected to the host aorta at the origin of the brachiocephalic artery. As a result, the jet flow from the aortic root impinged on the superior site of the arch along the anterior wall of the conduit, inducing recirculating flow in the lower region of the arch, which is undesirable and should be avoided. The length of the ascending aorta to be replaced by the conduit is determined by the distal involvement of aortic diseases.¹⁹ If the aortic disease affects the aortic arch, the entire ascending aorta, and even part of the arch, has to be replaced. It can be deduced that having a naturally curved conduit might help reduce the presence of recirculating flow in the arch and improve the overall flow performance in the aorta.

Limitations

The CFD models employed here assumed a rigid wall. Changes in aortic area were estimated based on MR data acquired at the two imaging planes for each subject, and these varied between 6-20% at the aortic root and between 10-15% in the descending aorta. The rigid wall assumption is likely to over-estimate the magnitude of WSS in systole and under-estimate HFI in diastole when compared to fluid-structure interaction (FSI) model.⁵ The effect of aortic wall compliance should be assessed in future studies using FSI simulations. The assumption of Newtonian fluid may also affect the magnitude of WSS and mass transport related parameters in the wall.²⁴

Conclusion

In summary, our detailed patient-specific analysis revealed that the overall flow patterns and average values of WSS in the aortas were comparable between patients following the composite valve-conduit implantation and normal subjects.

Minor differences were found in helical flow structure and spatial distribution of WSS, with the post-operative patients showing slightly reduced helical flow index and higher non-uniformity in wall shear. Different hemodynamic conditions were also noted among the patients, which were largely due to the geometric configuration of the conduit in the ascending aorta. The length and curvature of the conduit are believed to be key factors in determining post-operative aortic flow, and the overall performance of the root replacement procedure is likely to benefit from introducing a natural curvature in the conduit, but more studies are needed to confirm this hypothesis.

Acknowledgments

This work was supported by Vascutek Terumo, Renfrewshire, Scotland and the National Institute for Health Research Biomedical Research Centre based at Imperial College Healthcare NHS Trust and Imperial College London. The authors declare that although Vascutek Terumo partially supported this study, the funding company had no control, input or influence on the study design, data analysis or publications.

References

1. Barker AJ, Lanning C, Shandas R. Quantification of hemodynamic wall shear stress in patients with bicuspid aortic valve using phase-contrast MRI. *Ann Biomed Eng.* 2010; 38: 788-800.
2. Bentall H., Debono A. A technique for complete replacement of the ascending aorta. *Thorax* 1968; 23: 338-339.
3. Bochenek-Klimczyk K, Lau KK, Galinanes M, Sosnowski AW. Preassembled stentless valved-conduit for the replacement of the ascending aorta and aortic root. *Interact Cardiovasc Thorac Surg* 2008;7:964-968.

4. Borger MA, Carson SM, Ivanov J, Rao V, Scully HE, Feindel CM et al. Stentless aortic valves are hemodynamically superior to stented valves during mid-term follow-up: a large retrospective study. *Ann Thorac Surg* 2005;80:2180-2185.
5. Brown AG, Shi Y, Marzo A, Staicu C, Valverde I, Beerbaum P, Lawford PV, Hose DR. Accuracy vs. computational time: Translating aortic simulations to the clinic. *J Biomech* 2012;45:516-523.
6. Chatzizisis YS, Coskun AU, Jonas M, Edelman ER, Stone PH, Feldman CL. Risk Stratification of Individual Coronary Lesions Using Local Endothelial Shear Stress: A New Paradigm for Managing Coronary Artery Disease. *Curr Opin Cardiol* 2007; 22: 552-564.
7. Cheng Z. Analysis of blood flow in patient-specific models of type B aortic dissection. PhD Thesis. Imperial College London, 2012.
8. Cibis M, Potters WV, Gijzen FJ, Marquering H, vanBavel E, van der Steen AF, Nederveen AJ, Wentzel JJ. Wall shear stress calculations based on 3D cine phase contrast MRI and computational fluid dynamics: a comparison study in healthy carotid arteries. *NMR Biomed.* 2014;27:826-834
9. Davies JE, Parker KH, Francis DP, Hughes AD, Mayet J. What is the role of the aorta in directing coronary blood flow? *Heart.* 2008; 94:1545-1547.
10. Di Bartolomeo R, Botta L, Leone A, Pilato E, Martin-Suarez S, Bacchini M et al. Bio-Valsalva prosthesis: 'new' conduit for 'old' patients. *Interact Cardiovasc Thorac Surg* 2008;7:1062-1066.
11. Fedak PWM, Verma S, David TE, Leask RL, Weisel RD, Butany J. Clinical and Pathophysiological Implications of a Bicuspid Aortic Valve. *Circulation* 2002;106: 900-904.

12. Grigioni M, Daniele C, Morbiducci U, Del Gaudio C, D'Avenio G, Balducci A, Barbaro V. A mathematical description of blood spiral flow in vessels: application to a numerical study of flow in arterial bending. *J Biomech* 2005; 38(7): 1375-1386.
13. Hope TA, Markl M, Wigstrom L, Alley MT, Miller DC, Herfkens RJ. Comparison of flow patterns in ascending aortic aneurysms and volunteers using four-dimensional magnetic resonance velocity mapping. *J Magn Reson Imaging* 2007; 26(6): 1471-1479.
14. Kaya A, Heijmen RH, Kelder JC, Schepens MA, Morshuis WJ. Stentless biological valved conduit for aortic root replacement: Initial experience with the Shelhigh BioConduit model NR-2000C. *J Thorac Cardiovasc Surg* 2011;141:1157-1162.
15. Kaya A, Heijmen RH, Kelder JC, Morshuis WJ. First 102 patients with the BioValsalva conduit for aortic root replacement. *The Annals of thoracic surgery* 2012;94:72-77.
16. Kidher E, Cheng Z, Jarra OA, O'Regan DP, Xu XY, Athanasiou T. In-vivo assessment of the morphology and hemodynamic functions of the BioValsalva composite valve-conduit graft using cardiac magnetic resonance imaging and computational modelling technology. *J Cardiothorac Surg* 2014; 9: 193.
17. Kilner PJ, Yang GZ, Mohiaddin RH, Firmin DN, Longmore DB. Helical and retrograde secondary flow patterns in the aortic arch studied by three-directional magnetic resonance velocity mapping. *Circulation*. 1993;88(5):2235-2247.
18. Langtry, R. B. & Menter, F. R. Correlation-Based Transition Modeling for Unstructured Parallelized Computational Fluid Dynamics Codes. *AIAA Journal* 2009;47:2894-2906.

19. Lau KK, Bochenek-Klimczyk K, Galinanes M, Sosnowski AW. Replacement of the Ascending Aorta, Aortic Root, and Valve with a Novel Stentless Valved Conduit. *Ann Thorac Surg* 2008;86:278-281.
20. Lehoux S, Castier Y, Tedgui A. Molecular Mechanisms of the Vascular Responses to Hemodynamic Forces. *J Intern Med* 2006; 259: 381-392.
21. Li YSJ, Haga JH, Chien SS. Molecular Basis of the Effects of Shear Stress on Vascular Endothelial Cells. *J Biomech* 2005; 38: 1949-1971.
22. Lin AC, Lowe A, Sidhu K, Harrison W, Ruygrok P, Stewart R. Evaluation of a novel sphygmomanometer, which estimates central aortic blood pressure from analysis of brachial artery suprasystolic pressure waves. *J. Hypertens.* 2012; 30(9):1743-1750.
23. Liu X, Weale P, Reiter G, Kino A, Dill K, Gleason T, Carroll T, Carr J. Breathhold time-resolved three-directional MR velocity mapping of aortic flow in patients after aortic valve-sparing surgery. *J Magn Reson Imaging.* 2009;29(3):569-575.
24. Liu X, Fan Y, Deng X, Zhan F. Effect of non-Newtonian and pulsatile blood flow on mass transport in the human aorta. *J Biomech* 2011;44:1123-1131.
25. Liu X, Sun A, Fan Y, Deng X. Physiological significance of helical flow in the arterial system and its potential clinical applications. *Ann Biomed Eng* 2015;43: 3-15.
26. Markl M, Draney MT, Hope MD, Levin JM, Chan FP, Alley MT, Pelc NJ, Herfkens RJ. Time-Resolved 3-Dimensional Velocity Mapping in the Thoracic Aorta: Visualization of 3-Directional Blood Flow Patterns in Healthy Volunteers and Patients. *J Comput Assist Tomogr.* 2004;28(4):459-568.

27. Markwald RR, Norris RA, Moreno-Rodriguez R, Levine RA. Developmental basis of adult cardiovascular diseases: valvular heart diseases. *Ann N Y Acad Sci* 2010;1188:177–183.
28. Malek AM, Alper SL & Izumo S. Hemodynamic Shear Stress and Its Role in Atherosclerosis. *J Am Med Assoc* 1999; 282(21): 2035-2042.
29. Melina G, De Robertis F, Gaer JA, Amrani M, Khaghani A, Yacoub MH. Mid-term pattern of survival, hemodynamic performance and rate of complications after medtronic freestyle versus homograft full aortic root replacement: results from a prospective randomized trial. *J Heart Valve Dis* 2004;13:972-5; discussion 75-76.
30. Morbiducci U, Ponzini R, Rizzo G, Cadioli M, Esposito A, De Cobelli F, Del Maschio A, Montecvecchi FM, Redaelli A. In vivo quantification of helical blood flow in human aorta by time-resolved three-dimensional cine phase contrast magnetic resonance imaging. *Ann Biomed Eng* 2009; 37(3): 516-531.
31. Morbiducci U, Ponzini R, Rizzo G, Cadioli M, Esposito A, Montecvecchi FM, Redaelli A. Mechanistic insight into the physiological relevance of helical blood flow in the human aorta: an in vivo study. *Biomech Model Mechanobiol* 2011; 10(3): 339-355.
32. Morbiducci U, Ponzini R, Gallo D, Bignardi C, Rizzo G. Inflow boundary conditions for image-based computational hemodynamics: impact of idealized versus measured velocity profiles in the human aorta. *J Biomech* 2013; 46(1): 102-109.
33. Nishimura RA. Aortic Valve Disease. *Circulation* 2002;106:770-772.
34. Nkomo VT, Gardin JM, Skelton TN, Gottdiener JS, Scott CG, Enriquez-Sarano M. Burden of valvular heart diseases: a population-based study. *Lancet* 2006; 368:1005–1011.

35. Taylor CA, Steinman DA. Image-based modelling of blood flow and vessel wall dynamics: applications, methods and future directions. *Ann Biomed Eng* 2010; 38(3): 1188-1203.
36. Torii R, El-Hamamsy I, Donya M, Babu-Narayan SV, Ibrahim M, Kilner PJ, Mohiaddin RH, Xu XY, Yacoub MH. Integrated morphologic and functional assessment of the aortic root after different tissue valve root replacement procedures. *J Thorac Cardiovasc Surg*. 2012;143(6):1422-1428.
37. Zamir M, Sinclair P, Wonnacott TH. Relation between diameter and flow in major branches of the arch of the aorta. *J Biomech*. 1992; 25(11):1303-1310.
38. Zilla P, Bezuidenhout D, Human P. Prosthetic vascular grafts: wrong models, wrong questions and no healing. *Biomaterials* 2007; 28(34): 5009-5027.

Figure 1. (a) The BioValsalva valved conduit¹⁵; and the reconstructed aortic geometry of (b) normals and (c) patients with blue section representing the implanted conduit and red for the aorta.

Figure 2. The flow velocity profiles in three directions (FH, AP and RL) at the inlet, and pressure waveform at the outlet of each model. (a) and (b) are normals, (c)-(f) are four post-op patients. Velocity profiles are presented at five characteristic time points: T1 at mid-acceleration, T2 at peak systole, T3 at mid-deceleration, T4 at lowest flow rate, and T5 at mid-diastole.

Figure 3. Instantaneous streamlines in N1 at peak systole. Six planes are placed orthogonal to the centreline of the aorta as indicated, and velocity vectors are projected on the planes showing the in-plane velocity components with through-plane velocity contours. The centres of vortices are marked by stars.

Figure 4. Instantaneous streamlines in four patients at peak systole. Six planes are placed orthogonal to the centreline of the aorta of each patient as indicated, and velocity vectors are projected on the planes showing the in-plane velocity components with through-plane velocity contours. The centres of vortices are marked by stars.

Figure 5. (a) Traces of particle sets released at five injection phases T'_j in P1. The duration of trajectories is between the injection time and the end systole, and is coloured by the instantaneous value of LNH experienced by the moving particles (positive for right-handed, negative for left-handed). (b) Comparison of average values of HFI together with standard deviations between the normal and patient groups. HFI was calculated over the trajectory of particle sets at each of the five

injection time points respectively. (c) \overline{HFI} over particle sets released at five time points for each subject.

Figure 6. TAWSS contours on the aortic lumen wall. As indicated, (a) and (b) are normals and (c)-(f) are patients.

Figure 7. Variations of TAWSS, OSI and SRI along the aorta for normals and patients. The aorta is presented in sections including ascending aorta (AAo), aortic arch (AA), descending aorta (DAo), and BioValsalva conduit (BV) for patients.

Table 1: Averaged SRI, TAWSS and OSI along the aorta in different aortic sections,
and the tortuosity and aortic angle in normals and patients.

Variables	Normals			Patients				
	N1	N2	mean±SD	P1	P2	P3	P4	mean±SD
Tortuosity								
AAo [#]	1.47	1.38	1.43±0.06	1.28	1.36	1.31	1.50	1.36±0.10
Angle (°)								
BV* – AAo/AA ^Δ	-	-	-	106	115	111	91	105.75±10.5
AA – AAo	135	133	134±1.41	120	125	120	104	117.25±9.14
TAWSS (Pa)								
Max _{overall}	19.13	15.22	17.18±2.76	15.15	24	12.89	17.31	17.34±4.79
TAWSS _{mean} (Pa)								
BV	-	-	-	2.42	3.36	2.51	3.78	3.02±0.66
AAo	2.31	1.42	1.87±0.64	3.19	-	1.16	1.90	2.08±1.02
AA	3.05	0.58	1.82±1.75	2.08	5.30	1.57	1.05	2.50±1.91
DAo [§]	1.10	0.23	0.67±0.61	0.51	1.20	0.21	0.16	0.52±0.48
OSI _{mean}								
BV	-	-	-	0.17	0.17	0.14	0.11	0.15±0.03
AAo	0.14	0.19	0.16±0.04	0.13	-	0.21	0.13	0.16±0.05
AA	0.17	0.27	0.22±0.07	0.17	0.14	0.19	0.23	0.18±0.04
DAo	0.25	0.37	0.31±0.08	0.28	0.24	0.35	0.39	0.32±0.07
SRI								
BV	-	-	-	15.22	22.99	24.73	5.57	21.33±8.74
AAo	9.07	9.83	9.45±0.54	12.33	-	48.61	3.06	21.33±24.07
AA	15.68	11.03	13.35±3.29	5.81	25.31	13.87	8.88	13.47±8.57
DAo	9.24	11.42	10.33±1.54	7.81	5.27	18.77	17.23	12.27±6.73

*BioValsalva conduit section; #Ascending aorta section; ΔAortic arch section; §Descending aorta

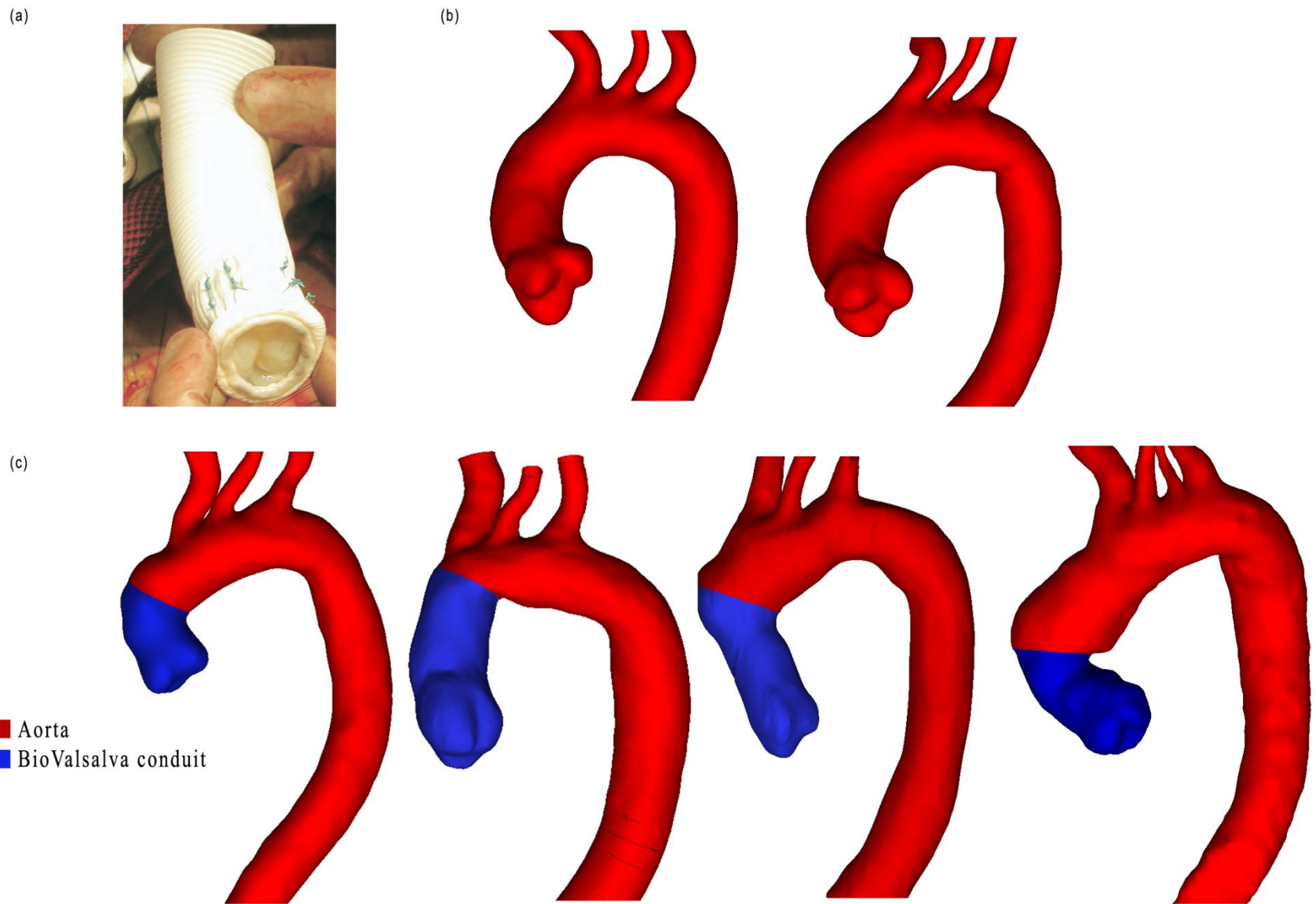


Figure 1

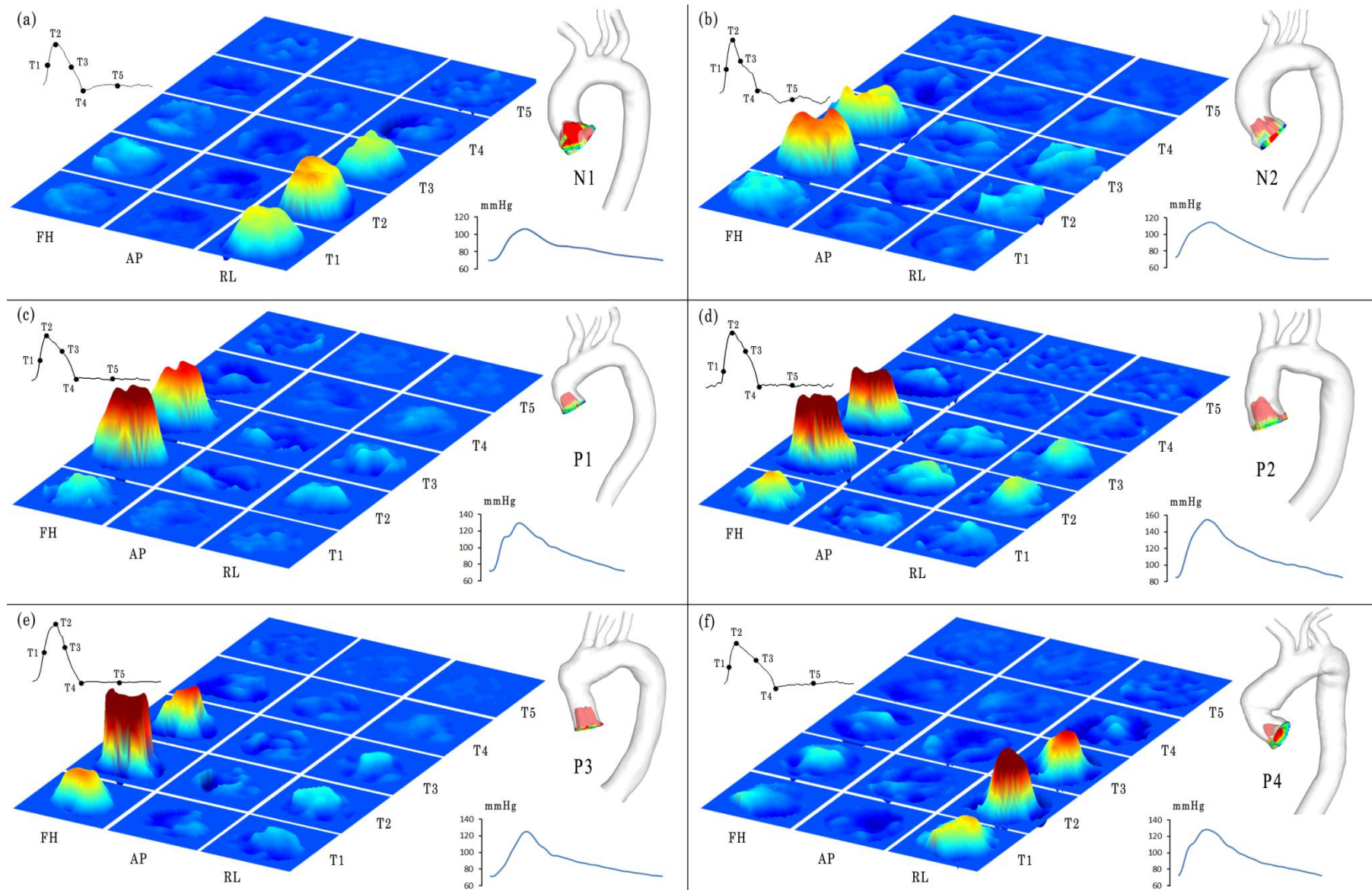


Figure 2

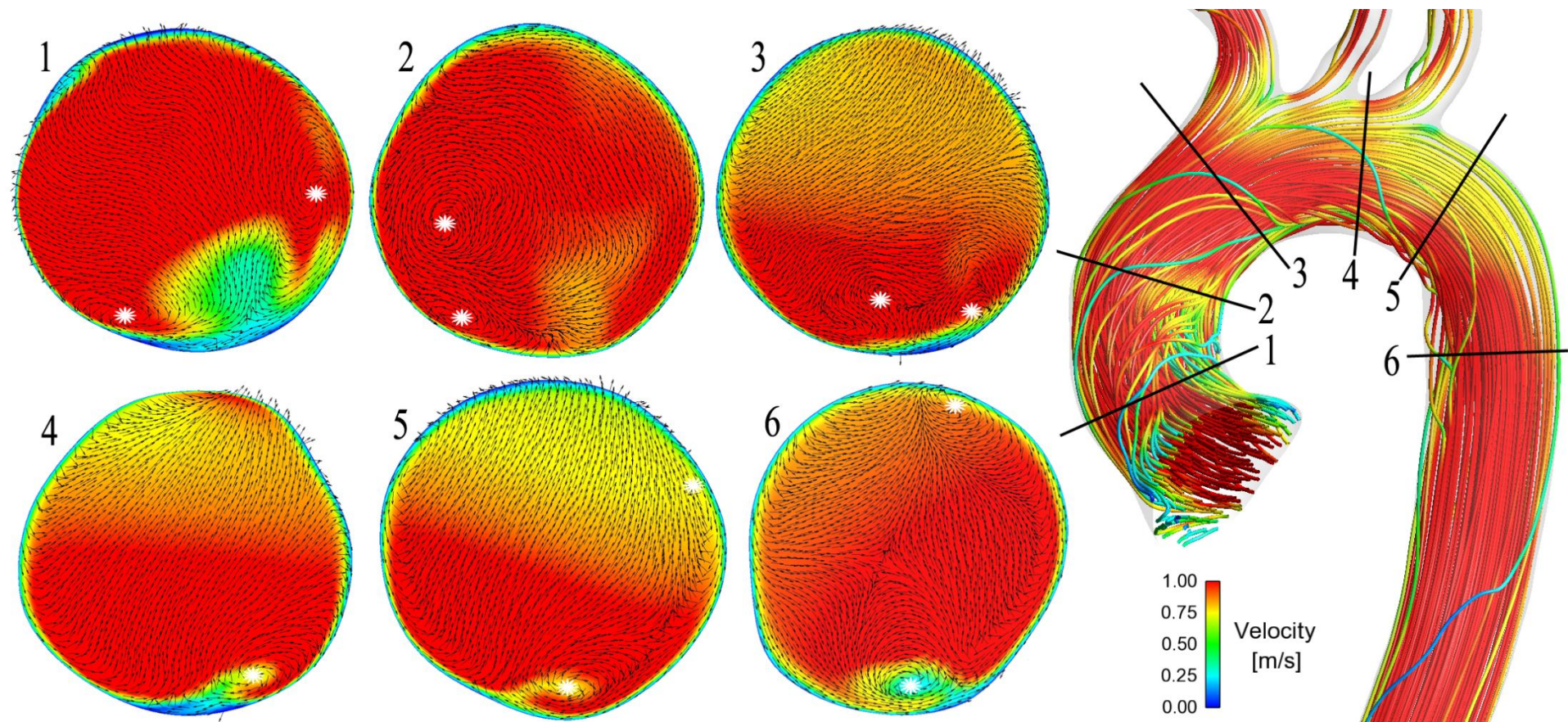


Figure 3

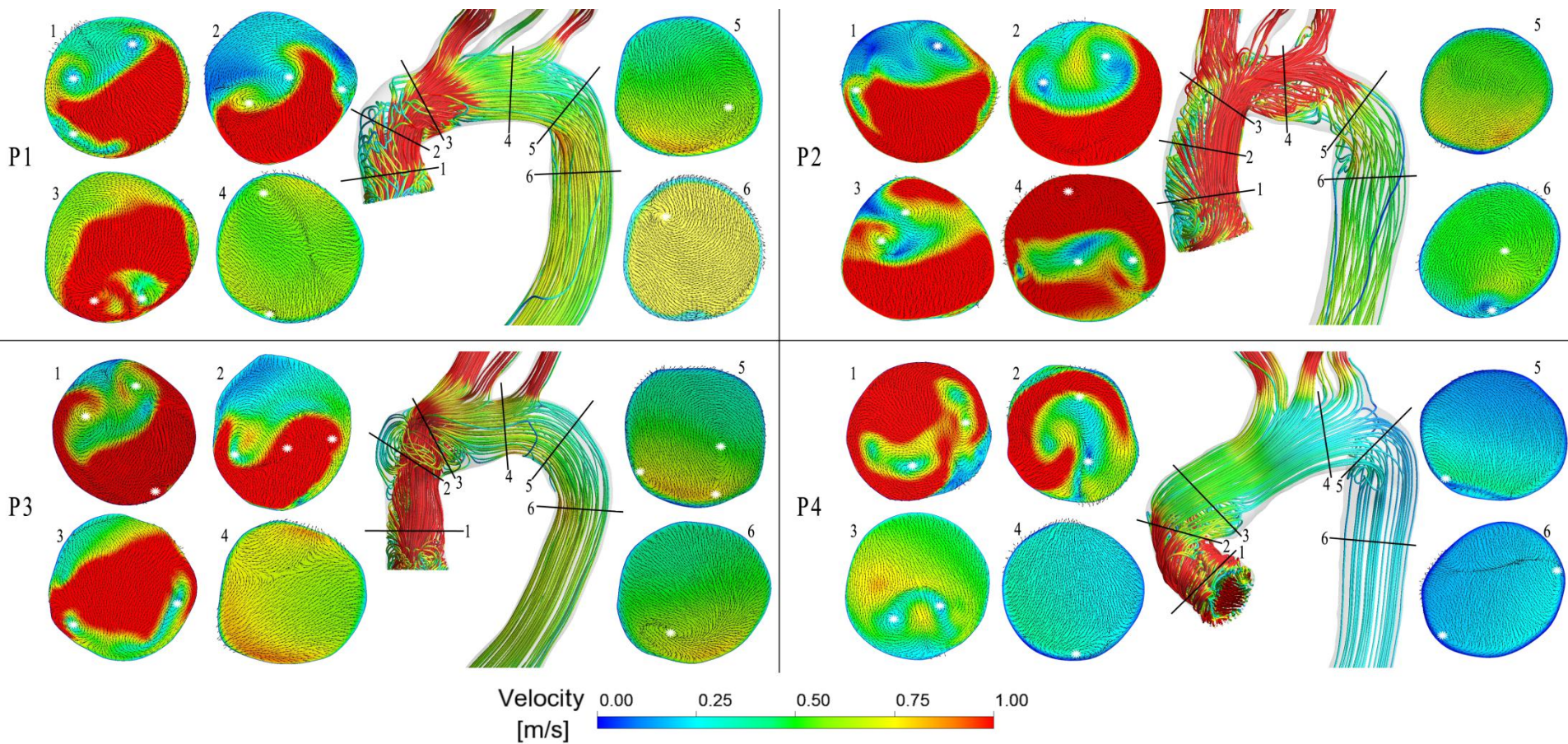


Figure 4

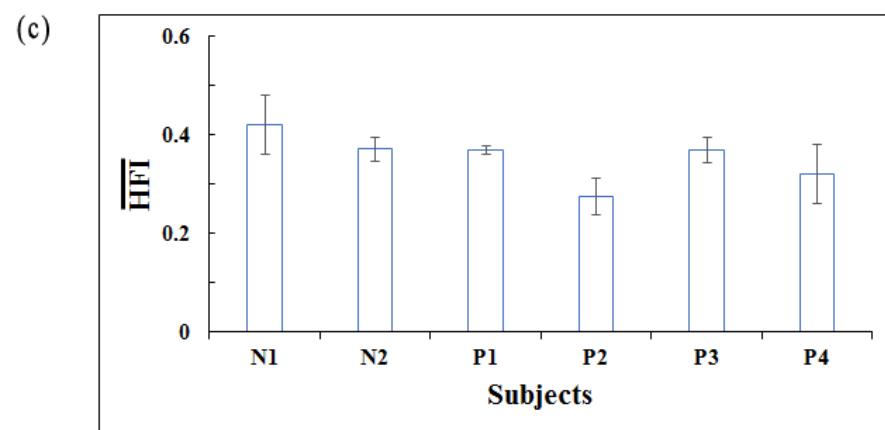
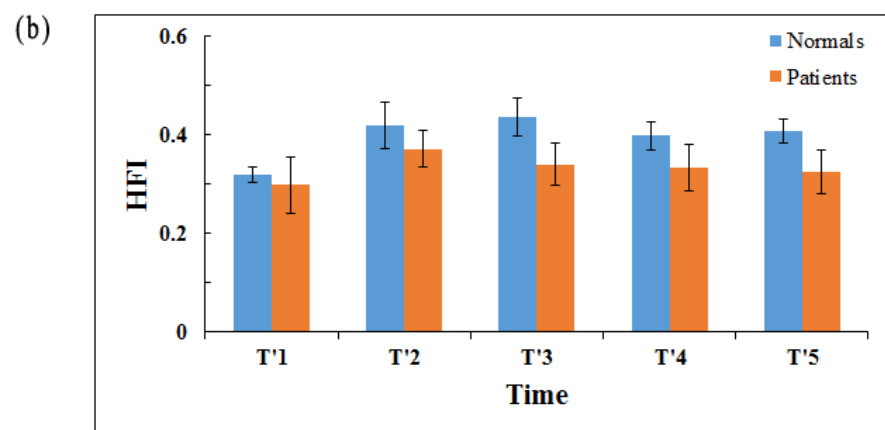
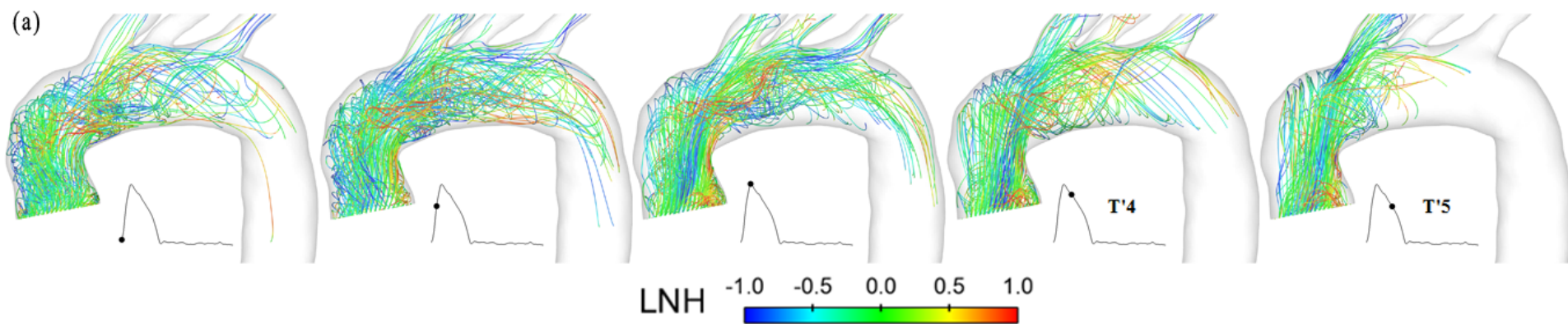


Figure 5

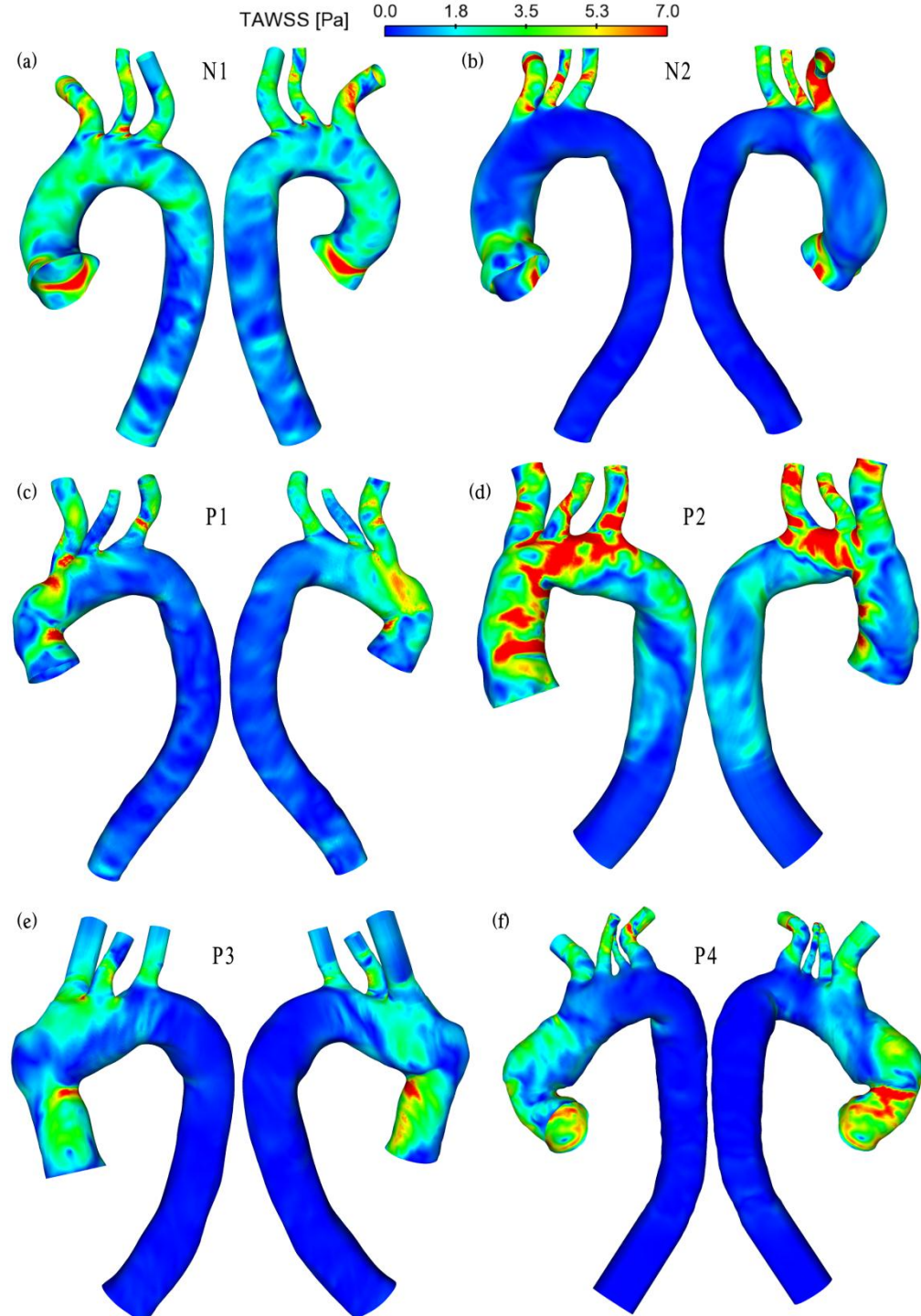


Figure 6

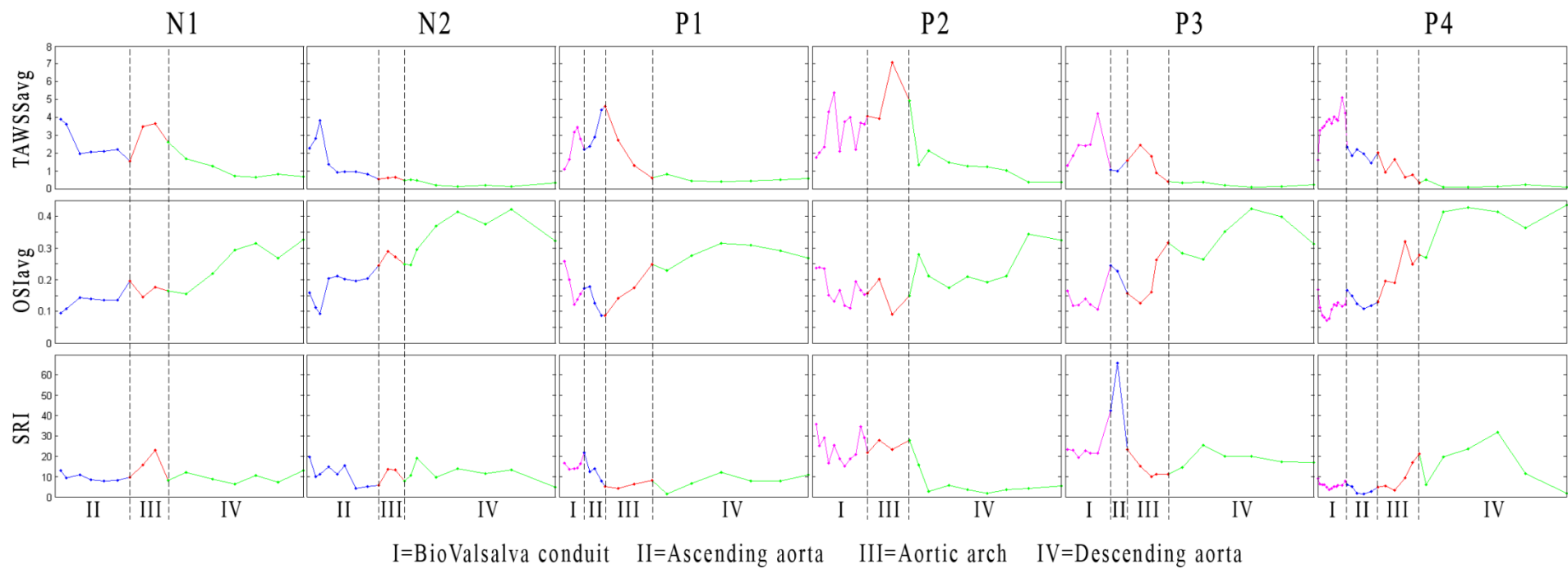


Figure 7